JOURNAL OF AIRCRAFT
Vol. 48, No. 1, January–February 2011

Coupled Multibody/Computational Fluid Dynamics Simulation of Maneuvering Flexible Aircraft

Luca Cavagna,* Pierangelo Masarati,† and Giuseppe Quaranta‡
Politecnico di Milano, 20156 Milan, Italy

DOI: 10.2514/1.C000253

This paper illustrates the application of multibody system dynamics coupled to computational fluid dynamics for the aeroelastic analysis of detailed aircraft models performing arbitrary free flight motion. An efficient alternative to modeling different aspects of aeromechanics in a monolithic code consists in building computational aeroservoelasticity modeling capability using independent software components for each domain: structure, fluid and mechanism analysis. This partitioned approach relies on dedicated software exploiting the most appropriate techniques to address the dynamics of each specific field. Efficiency is guaranteed since each subsystem can be modeled independently; specific time and spatial scales of interest are considered. Model setup is flexible: the designer can choose the most appropriate tools, trading accuracy for computational costs, requiring higher-order fidelity methods only when simplified ones cannot be applied, or their validation is pursued. The combination of multibody system dynamics and computational fluid dynamics yields a highly accurate prediction tool, that can be crucial in the preliminary and intermediate design steps of unconventional configurations, for the investigation of loads, performance, stability and vibratory response of the vehicle at the boundaries of the flight envelope. Its application to the analysis of an aircraft maneuvering in transonic flight is presented.

I. Introduction

WHEN structures are sufficiently rigid, aircraft dynamics dominated by rigid body motion are well separated from those dominated by structural deformation. As a consequence, vehicle dynamics modeling, analysis and synthesis usually focus either on rigid body or on structural dynamics, depending on the dominant system behavior.

When stability, controls and handling qualities are investigated, rigid body dynamics are often assumed. Similarly, when aeroelastic stability is addressed, rigid body motion is usually neglected.

The development of aircraft design benefited from significant weight saving and efficiency improvement resulting from multidisciplinary optimization procedures, extensive use of composite materials, exploitation of innovative layouts. As a consequence, aeroelastic effects tend to dominate the dynamic behavior of aircraft. Frequency separation between rigid and elastic modes tends to decrease, because larger and more slender designs result in lower frequencies of elastic modes. Moreover, increased authority and bandwidth of automatic flight control systems results in further reduction, or even in cancellation, of frequency separation between purely aeroelastic and flight mechanics related phenomena.

An integrated aeroservoelastic approach is required to take into account these analysis needs from the very beginning of the design process. Structural flexibility needs to be considered, although simplifications may be acceptable provided that they suit the particular needs of the application. A complex example of high-altitude low endurance flying wing aircraft is discussed by Patil and Hodges [1], where the dependence of the phugoid mode on the trim deformed shape, which may eventually become unstable, is outlined.

Different issues arise when the interaction between arbitrary rigid body motion and structural dynamics needs to be considered simultaneously. Many authors, since the first applications given by Ashley [2] and Milne [3,4], aimed at developing formulations as simple as possible, where rigid and deformable modes could be decoupled from an inertial standpoint. This turned out to be too limiting, since aerodynamic coupling could not be eliminated. Most formulations lead to nonlinear models; nonlinearity arises by combining the linear equations related to structural dynamics, often represented by normal vibration modes (e.g. Meirovitch [5]), with the nonlinear equations that govern the rigid body dynamics (e.g. Etkin [6]).

Models of this type are relatively accurate. They are widely used in many circumstances, especially when control is concerned. Applications can be found for example in Buttrill et al. [7], Waszak and Schmidt [8], Schmidt and Raney [9]. When flight stability and control are addressed, linearized models are used also for the rigid body terms, as in classic flight mechanics.

Issues arise when a unified formulation needs to be developed, combining methodologies typical of flight mechanics, structural dynamics, unsteady aerodynamics, and control. Applications of unified approaches can be found in Rodden and Love [10], Bianchin et al. [11], Baldelli et al. [12]. Linear flutter engineering models that incorporate rigid displacement and rotation degrees of freedom cannot recover traditional flight mechanics equations of motion because of inherently conflicting modeling objectives. These include the finite element (FE) model coordinate system, as opposed to "wind" axes, the unsteady modeling of the aerodynamic forces using pure harmonic motion from classic doublet lattice method, thus missing the reference loads the model is actually linearized about, and the lack of gravity-related terms. These deficiencies explain the differences observed in the eigenvalues associated with the free longitudinal and lateral dynamics modes obtained from traditional linear aeroelastic models.

A transformation process is usually required. This often caused misunderstandings between flight mechanists and aeroelasticians. The structural rigid body modes are transformed into the airframe states so that the definition of the rigid body motion for the aeroelastic system is consistent with that of flight dynamics. Typical aircraft rigid body motions, like short period, phugoid, and Dutch roll, are often described using quasi-steady aerodynamic forces (a reduced

Received 11 January 2010; revision received 14 June 2010; accepted for publication 21 October 2010.

*Ph.D., Dipartimento di Ingegneria Aerospaziale, Via La Masa, 34; luca.cavagna@polimi.it; currently at FOI (Swedish Defence Research Agency).

†Assistant Professor, Dipartimento di Ingegneria Aerospaziale, Via La Masa, 34; pierangelo.masarati@polimi.it.

‡Postdoctoral Research Fellow, Dipartimento di Ingegneria Aerospaziale, Via La Masa, 34; giuseppe.quaranta@polimi.it.

frequency domain series expansion of the unsteady aerodynamic forces about the null frequency), while aeroelasticity is usually based on unsteady models of aerodynamic forces. These forces are usually expressed in the structural coordinate frame for harmonic displacements and rotations. A transformation process is required to project them in the classic stability axes used in flight mechanics, where angles and velocities are adopted. The report by Meijer and Zwaan [13] addresses this point.

The coupling of dedicated fluid and structure solvers for aeroelastic analysis of maneuvers is a well established research topic for steady [14] and dynamic cases [15,16]. Current trends pursue the adoption of high fidelity methods, like computational fluid dynamics (CFD), especially when the prediction of aerodynamic loads for high-performing aircraft, featuring delta wings with vortices and separations, is concerned [17].

These designs are characterized by significant phase shifts between the deformation of the maneuvering aircraft and the distribution of aerodynamic loads. The integration of complex CFD models, flight mechanics and structural dynamics solvers is thus needed. Applications can be found in the work presented by Fornasier et al. [18], and Schütte et al. [19], where different kinds of models are coupled, e.g. CFD, FE and multibody system dynamics (MSD).

MSD represents a very versatile gluing tool as it allows the natural and straightforward coupling of flight mechanics into the aeroelastic simulation of free aircraft. Indeed, the multibody approach allows an efficient representation of the combination of elastic motion and arbitrary rotations. It is particularly suitable for multiphysics simulations with different types of nonlinearities. It allows to directly model structural dynamics, servo-systems, controls, nonlinearities like backlash, free-play, friction, and generic lumped nonlinearities in a single framework. Recent examples of aerospace applications can be found in [20–22].

MSD started as a general means to address the analysis of mechanisms essentially consisting of rigid bodies. A review of fundamental works in this area is provided by Schiehlen [23]. It was soon extended to flexible systems, essentially following two paradigms: initially, by superimposing linear FE modeling to arbitrary rigid body dynamics described by a floating frame; subsequently, by directly modeling nonlinear FEs within the multibody formalism, using absolute nodal coordinates, as illustrated by Shabana [24].

Usually, structural models are reduced as much as possible, compatibly with reproducing the physics of the problem within the desired accuracy. Compared with typical FE models for dynamics analysis, quite simple models are often used. They range from lumped masses and springs, to component mode synthesis (CMS) models, based on the combination of normal vibration modes and static shapes with reference arbitrary motion provided by a floating frame, and to geometrically nonlinear FEs in absolute coordinates, typically using beam or, in specific cases, shell elements.

In aeromechanics and aeroelasticity, MSD is especially suitable for preliminary design, because it allows a medium level of complexity in structural modeling. Examples of application of MSD to the analysis of the maneuvering aircraft can be found in Spieck et al. [21] and Krüger et al. [22]. Applications to rotorcraft aeroelasticity can be found in Zaki et al. [25] and Yeo et al. [26]. These works present the coupling between a multibody solver and different low/high fidelity methods for aerodynamics.

This work illustrates a tight fluid–structure interaction (FSI) approach based on the simultaneous solution of CFD and MSD subproblems addressing deformable transonic aircraft in maneuver flight. The focus is on aeroelastic stability in free flight conditions. Examples from the literature and the analysis of an application of industrial interest (the Piaggio P180 general aviation aircraft) show the soundness of the approach.

II. Approach

The floating frame approach is adopted to describe arbitrary rigid body motion in not necessarily attached body-reference axes. While body-fixed axes are commonly used for rigid bodies, a moving floating frame is usually adopted for deformable bodies. It is worth mentioning that many of the concepts used in the floating frame formulation were originally presented in the aerospace literature.

According to Agrawal and Shabana [27], two sets of coordinates are used to describe the configuration of the deformable body: the motion of the reference frame, represented by a set of Cartesian coordinates and rotational parameters, and the deformation of the body, described by a set of generalized coordinates, with respect to the moving reference coordinate system. The latter contribution can directly originate from FE, or result from model reduction, e.g., through CMS.

The equations of motion of deformable bodies that undergo arbitrary rigid body motion are highly nonlinear, and may exhibit strong nonlinear couplings. Compared with rigid body problems, deformation modeling is of major concern. A comparatively large number of deformable degrees of freedom may be required for acceptable accuracy. However, different arrangements can be selected for the body axes of flexible components. A possible choice is represented by the Tisserand or Buckens (mean axes) frames [28]. To uniquely define a displacement field, a set of reference conditions defining the nature of the body axes needs to be imposed. The deformation shapes of the body are indeed defined in the coordinate system of the body itself. Consequently, the selection of the deformation shapes and of the body coordinate system are closely related.

A dynamics analysis application based on Ritz method is presented by Wallrapp and Wiedemann [29]. The work simulates the deployment of a flexible solar array. The choice of an appropriate set of shape functions is addressed. Different eigenmodes and static shapes are selected using a modal participation factor criterion to improve the convergence of the method. The choice is not trivial: it strictly depends on the loading cases that need to be considered. In Wallrapp and Wiedemann [30], different choices for the basis functions are outlined. Schwertassek et al. [31] outline the mathematical formulation given by a combination of MSD and FE.

In the present work, the modeling of the arbitrary reference motion of the aircraft is delegated to the free general-purpose multibody dynamics solver MBDyn.[§] MBDyn can directly model the structural deformation, either by CMS, with data obtained from FE, or directly, by built-in nonlinear beam FE [32].

Nowadays, CFD is a consolidated technology for aerodynamics analysis, with several advantages. It allows to set up models with different levels of accuracy (typically compressible Euler or Navier–Stokes equations with turbulence modeling) that are suitable for the examined flight condition. Thus, it allows to trade cost and accuracy depending on mesh resolution, flow model and spatial and temporal scales of interest. High-fidelity simulations coupled to rigid body motion allow to accurately estimate stability and control characteristics [33]. They contribute to reduce wind-tunnel and flight testing for a new design or a new configuration to be cleared, reducing time-to-market and undesirable flight envelope restrictions. CFD models are intrinsically unsteady; they allow the direct simulation of dynamic flow phenomena and coupled dynamic response, as is the case of FSI. This allows to consider the propagation of the response in the flow, i.e., response to external disturbance like gusts or moving boundaries and their interaction with shocks leading to the transonic dip [34].

Current regulations require to consider transient loads "where structural flexibility is such that any rate of load application likely to occur in the operating conditions might produce transient stresses appreciably higher than those corresponding to static loads" (CS 25.305 [35]).

Complex flow models, like those based on Navier–Stokes equations, allow to investigate complex phenomena like buzz, buffet, limit cycle oscillations (LCO), mainly governed by flow nonlinearities, e.g., separations, vortex flows interactions and shock-induced separations [36].

Section VIII shows how the motion of the control surfaces, along with structural deformation, can significantly change the flow field.

[§]Available at http://www.mbdyn.org/ [retrieved Nov. 2010].

This is known to impact the aeroelastic stability of the system [37]. Even static loads may significantly impact the aeroelastic stability of aircraft. For example, positive dihedral angle of T-tail designs has a destabilizing effect on stability (Land and Fox [38]). The effective dihedral resulting from the static deformation of the stabilizer under load introduces an additional dependence of the linearized equations on the aeroelastic equilibrium state (Jennings and Berry [39]).

The use of CFD in aeroservoelasticity is usually related to deformable aircraft models based on FE analysis, often reduced by CMS, or even on modal survey by ground vibration testing (GVT) [40]. The CFD solver "Edge" [41], developed by FOI (Swedish Defence Research Agency), is used to compute the unsteady aerodynamic loads based on several models, ranging from Euler equations to complex turbulent flows (Reynolds-averaged Navier–Stokes, detached-eddy simulation, and large-eddy simulations).

A key issue of using CFD for aeroservoelasticity is related to finding a trade-off between the high computational cost and the need to perform aeroelastic computations in the time domain. Unsteadiness may considerably add to the computational complexity of the fluid dynamics simulation. This is particularly true when unsteady maneuvering conditions need to be addressed, since the duration of the analysis may grow significantly; the time scale of maneuvers ranges from few seconds to minutes. The formulation of each solver (implicit/explicit) and the coupling approach are indeed of primary importance for multiphysics analyses.

Dealing with free-free deformable mechanisms requires the capability to describe the arbitrary global motion of the aircraft subjected to aerodynamics forces and moments, along with the deformability of the structure. In this sense, the use of the floating mean reference frame helps the designer in forcing the trajectory of the aircraft or to determine its gross motion while subjected to deformation.

This work outlines the choice of the reference frame for the deformable aircraft and the conservation laws of fluids with deformable computational domains for CFD applications using the arbitrary Lagrangian Eulerian (ALE) formulation (see Donea and Huerta [42] for example).

The coupled system is solved to determine the stationary trim solution for the free flying aircraft. The reference motion can be directly specified as boundary condition to the CFD solver, and the structural deformation can be addressed by deforming the CFD mesh. An efficient alternative is represented by the modification of the velocity boundary conditions according to the so-called "transpiration" method, under the assumption of limited structural deformation. The latter solution does not require CFD grid deformation, which is a critical and time consuming task related to fluid dynamics computation, thus drastically improving the efficiency of the coupling. Fisher and Arena [43] discuss its application to computational aeroelasticity based on CFD.

A tightly coupled approach is pursued in this work. It consists in bringing the mechanical and aerodynamic analyses to convergence simultaneously for each time step. This aspect can be quite important when significant structural deformation needs to be addressed (e.g. for high aspect ratio configurations), if the frequency band of the structure, including control surface actuators, is relatively high. In this type of problems, the introduction of numerical time lag and spurious work contribution must be strictly avoided.

III. Multibody Solver MBDyn

THE structural modeling is delegated to the free general-purpose multibody solver MBDyn, developed at the Dipartimento di Ingegneria Aerospaziale of the University Politecnico di Milano. It is designed to model generic multidisciplinary problems, characterized by "exact" constrained rigid body dynamics, deformable components, either directly modeled as nonlinear FE or through CMS, simplified aerodynamics, controls and more. MBDyn solves initial value problems in form of differential-algebraic equations, using a family of multistep L-stable integration algorithms, with algorithmic dissipation [44].

Newton–Euler equations describe the motion of a set of rigid bodies, constrained using Lagrange's multipliers. The equations of motion of the i-th node are written in first-order form by adding the definitions of the momentum, $\boldsymbol{\beta}_i$, and of the momenta moments, $\boldsymbol{\gamma}_{i\mathbf{x}_i}$, with respect to the position of the node, $\mathbf{x}_i$, namely

$$m_i\dot{\mathbf{x}}_i + \boldsymbol{\omega}_i \times \mathbf{S}_{i\mathbf{x}_i} = \boldsymbol{\beta}_i \tag{1a}$$

$$\mathbf{S}_{i\mathbf{x}_i} \times \dot{\mathbf{x}}_i + \mathbf{J}_{i\mathbf{x}_i}\boldsymbol{\omega}_i = \boldsymbol{\gamma}_{i\mathbf{x}_i} \tag{1b}$$

where m_i is the mass, $\boldsymbol{\omega}_i$ is the angular velocity, and $\mathbf{S}_{i\mathbf{x}_i}$ and $\mathbf{J}_{i\mathbf{x}_i}$ are the first- and second-order inertia moments. The equilibrium of each node is

$$\dot{\boldsymbol{\beta}}_i = \sum \mathbf{f}_i \tag{2a}$$

$$\dot{\boldsymbol{\gamma}}_{i\mathbf{x}_i} + \dot{\mathbf{x}}_i \times \boldsymbol{\beta}_i = \sum \mathbf{m}_{i\mathbf{x}_i} \tag{2b}$$

where $\mathbf{f}_i$ and $\mathbf{m}_{i\mathbf{x}_i}$ are all the remaining forces and moments about the node acting on the body. The unconstrained equations of motion of all the nodes can be summarized as

$$\mathbf{M}\,\dot{\mathbf{q}} = \mathbf{p} \tag{3a}$$

$$\dot{\mathbf{p}} = \mathbf{f}(\mathbf{q}, \dot{\mathbf{q}}, \mathbf{p}, t) \tag{3b}$$

where $\mathbf{q} \in \mathbb{R}^n$ summarizes the n coordinates of the system,[¶] $\mathbf{M} \in \mathbb{R}^{n\times n}$ is the mass matrix, $\mathbf{p} \in \mathbb{R}^n$ summarizes momentum and momenta moments, and $\mathbf{f}$: $\mathbb{R}^{3n+1} \mapsto \mathbb{R}^n$ summarizes the generic forces, possibly depending on the configuration of the system.

When the system is subjected to kinematic constraints, the c holonomic constraint equations $\boldsymbol{\phi}(\mathbf{q}, t)$: $\mathbb{R}^{n+1} \mapsto \mathbb{R}^c$ are added to Eqs. (3) using Lagrange's multipliers $\boldsymbol{\lambda}$, resulting in

$$\mathbf{M}\,\dot{\mathbf{q}} = \mathbf{p} \tag{4a}$$

$$\dot{\mathbf{p}} + \boldsymbol{\phi}_{/\mathbf{q}}^T\boldsymbol{\lambda} = \mathbf{f}(\mathbf{q}, \dot{\mathbf{q}}, \mathbf{p}, t) \tag{4b}$$

$$\boldsymbol{\phi}\,(\mathbf{q}, t) = \mathbf{0} \tag{4c}$$

Nonholonomic constraints are dealt with similarly.

The CMS approach is not described in detail, as it is a consolidated technique to capture the dynamics of large complex deformable subsystems in reduced order, yet extremely efficient models [24,45,46]. In the present case it is used to describe the dynamics of an entire free flying aircraft using a limited number of normal vibration modes. Model data is usually extracted from large FE models. Data can also be obtained from GVT performed on the real aircraft, as in this work (see Sec. VIII). The CMS model is based on a description of the kinematics that consists in superimposing an elastic motion, $\tilde{\mathbf{R}}, \tilde{\mathbf{x}}$, to an arbitrary rigid body motion, $\mathbf{R}_O, \mathbf{x}_O$, of the reference system the elastic motion is referred to. The motion of an arbitrary point j is

$$\mathbf{R}_j = \mathbf{R}_O\tilde{\mathbf{R}}_j \tag{5a}$$

$$\mathbf{x}_j = \mathbf{x}_O + \mathbf{R}_O\tilde{\mathbf{x}}_j \tag{5b}$$

When the elastic motion is expressed as a linear combination of modes $\mathbf{u}$ through the modal rotation and displacement matrices, $\boldsymbol{\Psi}_{\mathbf{R}_j}$ and $\boldsymbol{\Psi}_{\mathbf{x}_j}$, namely $\tilde{\mathbf{R}}_j \cong \mathbf{I} + (\boldsymbol{\Psi}_{\mathbf{R}_j}\mathbf{u})\times$, $\tilde{\mathbf{x}}_j = \tilde{\mathbf{x}}_{j0} + \boldsymbol{\Psi}_{\mathbf{x}_j}\mathbf{u}$, Eqs. (5) become

[¶]For the sake of conciseness, this notation overlooks the fact that the angular rate $\boldsymbol{\omega}_i$ is not the derivative of the vectorial orientation parametrization $\mathbf{g}_i$, namely $\boldsymbol{\omega}_i = ax(\dot{\mathbf{R}}_i\mathbf{R}_i^T) = \mathbf{G}(\mathbf{g}_i)\dot{\mathbf{g}}_i$.

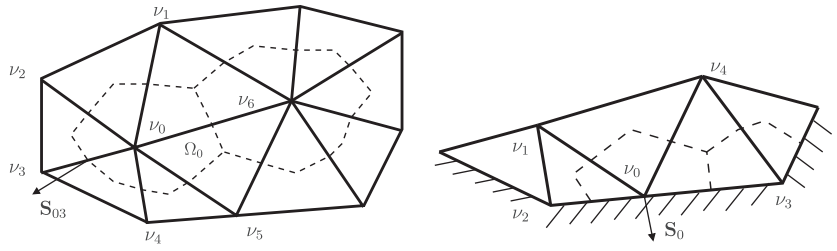

a) Internal nodes **b) Boundary nodes**

Fig. 1 Input grid (solid) and its dual grid (dashed) forming the control volumes for a two-dimensional case.

$$\mathbf{R}_j \cong \mathbf{R}_O(\mathbf{I} + (\boldsymbol{\Psi}_{\mathbf{R}_j}\mathbf{u})\times) \tag{6a}$$

$$\mathbf{x}_j = \mathbf{x}_O + \mathbf{R}_O(\tilde{\mathbf{x}}_{j0} + \boldsymbol{\Psi}_{\mathbf{x}_j}\mathbf{u}) \tag{6b}$$

Matrix $\tilde{\mathbf{R}}_j$ is only a first-order approximation of an orientation matrix, since $\tilde{\mathbf{R}}_j\tilde{\mathbf{R}}_j^T - \mathbf{I} = O(\|\mathbf{u}\|^2)$. Exploiting the principle of virtual work (PVW), the contribution of the internal (e.g. elastic) and external (e.g. inertial and dead) forces to the work done by the system for a virtual motion (i.e. infinitesimal and compatible with the constraints at fixed time) yields the equations of motion of the CMS element. Two main contributions result: one is associated to a virtual variation of the rigid body motion of the reference system, $\delta\mathbf{x}_O$, $\boldsymbol{\theta}_{O\delta}$ (since $\delta\mathbf{R}_O = \boldsymbol{\theta}_{O\delta} \times \mathbf{R}_O$), which accounts for the overall inertia of the system with no participation of elastic forces; the other is associated to a virtual variation of the straining of the system, $\delta\mathbf{u}$. They are summarized as

$$\begin{bmatrix} \mathbf{M_{xx}} & \mathbf{M_{x\theta}} & \mathbf{M_{xu}} \\ & \mathbf{M_{\theta\theta}} & \mathbf{M_{\theta u}} \\ \text{sym.} & & \mathbf{M_{uu}} \end{bmatrix} \begin{Bmatrix} \ddot{\mathbf{x}}_O \\ \dot{\boldsymbol{\omega}}_O \\ \ddot{\mathbf{u}} \end{Bmatrix} + \begin{bmatrix} \mathbf{0} \\ \mathbf{0} \\ \mathbf{K_{uu}} \end{bmatrix} \mathbf{u} + \begin{Bmatrix} \text{Coriolis} \\ \& \\ \text{centrifugal} \end{Bmatrix} = \begin{Bmatrix} \sum \mathbf{f_x} \\ \sum \mathbf{m}_{O\theta} \\ \sum \mathbf{f_u} \end{Bmatrix} \tag{7}$$

Submatrices $\mathbf{M}_{(\cdot)(\cdot)}$ and the Coriolis and centrifugal terms of Eq. (7) are usually expressed as functions of the so-called *inertia invariants* [45]. They represent a series expansion of the inertia of the system in terms of the modal variables $\mathbf{u}$ that allow to express the inertia forces as functions of the deformed state of the CMS element, provided appropriate information about the mass distribution is available.

To interact with the multibody domain, the CMS element needs to export its motion and receive forces at specific interface points. This is particularly useful, for example, to add the dynamics of hydraulic actuators, free-play and other nonlinearities to the modeling of aerodynamic control surfaces. To minimize software development and provide a generic interface, selected nodes of the CMS element can act as interface points. Constraint equations between their motion and that of corresponding multibody nodes are added using Lagrange's multipliers. For example, the j-th node of the FE mesh, whose motion depends on the CMS variables $\mathbf{u}$, interfaces with the i-th MSD node by explicitly enforcing the six algebraic Eqs. (6).

IV. Flow Solver Edge

Edge** is a CFD flow solver developed and maintained by FOI. It solves two- and three-dimensional viscous/inviscid, compressible flow problems on unstructured grids with arbitrary elements. An edge-based finite volume formulation is adopted where control volumes are cells of a dual mesh. Each cell contains a node of the primary grid where flow unknowns are evaluated (see Fig. 1). The dual mesh structure is generated by Edge's preprocessor. It also performs agglomeration of control volumes into coarser grids for multigrid. For parallel calculations, the mesh is partitioned using an optimal domain decomposition method.

Edge can be used for both steady state and time-accurate calculations, including maneuvers (Forsberg et al. [47]) and aeroelastic simulations (Girodroux-Lavigne et al. [48]). Applications of the solver also consider advanced turbulence modeling (Peng [49]) and shape optimization and flow control (Amoignon et al. [50]). An inviscid adjoint flow solver allows gradient based shape optimization and mesh adaptation techniques (Tysell [51]). An overview of typical applications is presented by Eliasson and Weinerfelt [41]. Theoretical details about the available numerical schemes are given by Eliasson [52].

The fluid dynamics problem is stated using an ALE formulation to represent the motion of the fluid mesh [42]. The integral form of the compressible unsteady Euler equations for each control volume $\Omega_i(t)$ with boundary $\partial\Omega_i(t)$ subjected to deformation is

$$\frac{\mathrm{d}}{\mathrm{d}t}\int_{\Omega_i(t)} \mathbf{w}\,\mathrm{d}V = -\oint_{\partial\Omega_i(t)} (\boldsymbol{\varphi}(\mathbf{w}) - \mathbf{w}\dot{\mathbf{x}}_f)\cdot\mathrm{d}\mathbf{S} \tag{8}$$

where $\mathbf{w} = (\rho, \mathbf{m}, E^t)^T$ are the usual conservative variables: the density ρ, momentum $\mathbf{m} \in \mathbb{R}^3$, and total energy per unit volume E^t; $\boldsymbol{\varphi} = (\varphi_x, \varphi_y, \varphi_z)^T \in \mathbb{R}^5 \mapsto \mathbb{R}^3$ are the inviscid fluxes, and $\dot{\mathbf{x}}_f(\mathbf{s}, t)$ is the local velocity of the moving boundaries of the mesh elements, which is a function of the curvilinear coordinate $\mathbf{s}$. The term $\mathbf{w}\dot{\mathbf{x}}_f$ accounts for the flux contribution due to the motion of the control volume. Equation (8) is also valid for the limit case of fixed grid, with $\dot{\mathbf{x}}_f = 0$ and constant volume $\Omega_i(t)$. The flux function is

$$\boldsymbol{\varphi}(\mathbf{w}) = (\mathbf{m}, \mathbf{m}\otimes\mathbf{m}/\rho + p(\mathbf{w})\mathbf{I}, (E^t + p(\mathbf{w}))\mathbf{m}/\rho^T \tag{9}$$

where p is the pressure. The addition of diffusive fluxes yields Navier–Stokes' model. The scalar product in Eq. (8) is computed as $\boldsymbol{\varphi}\cdot\mathrm{d}\mathbf{S} = \varphi_x\,\mathrm{d}S_x + \varphi_y\,\mathrm{d}S_y + \varphi_z\,\mathrm{d}S_z$, where $\mathrm{d}\mathbf{S}(\mathbf{s}, t)$ is the outward normal with respect to the volume $\Omega_i(t)$. The discrete formulation for Eq. (8) is

$$\frac{\mathrm{d}(\Omega_i\mathbf{w}_i)}{\mathrm{d}t} = \sum_{k\in\mathcal{T}_i} \boldsymbol{\Phi}(\mathbf{w}_i, \mathbf{w}_k, \mathbf{S}_{ik}, \mu_{ik}) + \boldsymbol{\Phi}^{\partial}(\mathbf{w}_i, \mathbf{S}_i, \mu_i) \tag{10}$$

where $\mathcal{T}_i$ is the set of nodes k sharing a portion of their boundary with the volume of node i, $\boldsymbol{\Phi}$ is the discrete form of the flux $\boldsymbol{\varphi}$, $\mathbf{S}_{ik}$ is the integrated outward normal related to the pair of nodes i, k (Fig. 1a), i.e. $\mathbf{S}_{ik} = \int_{\partial\Omega_{ik}(t)} \mathrm{d}\mathbf{S}_i(\mathbf{s}, t)$, and μ_{ik} is the integrated interface velocity $\mu_{ik} = \int_{\partial\Omega_{ik}(t)} \dot{\mathbf{x}}_f \cdot \mathrm{d}\mathbf{S}_i(\mathbf{s}, t)$. For numerical stability, the grid velocities μ_{ik} and the grid-dependent geometric quantities, like the volume associated to the finite volume of the integrated outward normals, need to comply with the constraints of the geometric conservation law (Thomas and Lombard [53]). In Edge, the numeric flux $\boldsymbol{\Phi}$ can be evaluated using central schemes with additional dissipation or Roe flux difference splitting. According to the piecewise representation of finite-volumes, the flux boundary contribution on the frontiers of the computational domain (see Fig. 1b) is

$$\boldsymbol{\Phi}^{\partial}(\mathbf{w}_i, \mathbf{S}_i, \mu_i) = \boldsymbol{\varphi}(\mathbf{w}_i)\cdot\mathbf{S}_i - \mathbf{w}_i\mu_i \tag{11}$$

In case of slip wall boundary, $\mathbf{w}_i$ is updated to account for zero relative velocity normal to the boundary.

**Available at http://www.foi.se/edge [retrieved Nov. 2010].

The flow equations are integrated using an explicit multistage Runge–Kutta scheme with convergence acceleration by multigrid agglomeration and implicit residual smoothing. Time-accurate solutions are obtained using an implicit dual time-stepping technique with explicit subiterations and a three-point backward differences formula:

$$\frac{\mathrm{d}(\Omega_i^* \mathbf{w}_i^*)}{\mathrm{d}\tau} = \tilde{\mathbf{\Phi}}(\mathbf{w}^*, \mathbf{S}_{ik}^*, \mu_{ik}^*) + \mathbf{Q} \tag{12}$$

with the unsteady residual:

$$\tilde{\mathbf{\Phi}}(\mathbf{w}^*, \mathbf{S}_{ik}^*, \dot{\mathbf{x}}^*) = -\frac{3\Omega_i^* \mathbf{w}^*}{2\Delta t} + \sum_{k \in \mathcal{T}_i} \mathbf{\Phi}(\mathbf{w}_i^*, \mathbf{w}_k^*, \mathbf{S}_{ik}^*, \mu_{ik}^*) + \mathbf{\Phi}^{\partial}(\mathbf{w}_i^*, \mathbf{S}_i^*, \mu_i^*) \tag{13}$$

where the superscript $(\cdot)^*$ indicates the variables during the pseudotime subiteration, and the constant source term:

$$\mathbf{Q} = \frac{4\Omega_i^{(n)} \mathbf{w}^{(n)} - \Omega_i^{(n-1)} \mathbf{w}^{(n-1)}}{2\Delta t} \tag{14}$$

The steady solution of Eq. (12) corresponds to the flow variables at the new time level, namely $\mathbf{w}^* = \mathbf{w}^{n+1}$. Since the residual is driven to zero at steady state in pseudotime, i.e. $\mathrm{d}(\cdot)/\mathrm{d}\tau = 0$, Eq. (10) is fulfilled. During iterative solution in pseudotime, data is exchanged with the MSD solver (see Sec. VI) to implement a fully-coupled approach that results in overall convergence of the monolithic problem.

The computational domain needs to be updated to correctly match the deformed structural shape. This typically requires either interpolation (e.g., Bartels [54] and de Boer et al. [55]), or mesh-deformation techniques (Zeng and Ethier [56] and Cavagna et al. [40]) to propagate the displacement of the moving boundaries through the entire internal mesh. Usually, accomplishing this task is computationally demanding and not trivial because mesh distortion and invalidation must be prevented.

Dating back to classic linear panel methods, a naïve approach called *transpiration* was developed. In case of small structural displacements, this approach allows to avoid the complexity of mesh-deformation. Initial applications in CFD-based aeroelastic analysis were related to full potential and Euler formulations; see for example Fisher and Arena [43], Stephens et al. [57,58], and Gao et al. [59], where the transpiration boundary condition is used as a linearized first-order wall boundary condition under the assumption of relatively small deformations. An additional benefit of this approach in aeroservoelasticity is related to control surfaces modeling, a fundamental issue whose modeling inside the CFD domain is not trivial. If narrow gaps are modeled, the number of elements in the domain increases, and issues in mesh-deformation may arise. If the control surface is incorporated into the wing boundary, a mesh shearing problem can result along the boundary edges the surfaces share, where a gap would need to appear. This phenomenon can lead to highly distorted grids and loss of mesh refinement in an area where flow gradients can actually be high.

The implementation of the transpiration boundary condition is straightforward. When the structure strains, as sketched in Fig. 2, each wall boundary is subjected to a normal variation from $\mathbf{S}_u$ to $\mathbf{S}_d$, describing the displacement of its nodes in the body-reference frame $\tilde{\mathbf{x}}$. This represents a geometric transpiration contribution. It needs to be considered any time the structural motion implies a change of the direction of boundary normals. Thus, when inviscid fluid models are used, the new deformed shape can be simulated by enforcing flow tangency of the flow velocity $\mathbf{v}_i$ using the deformed normal unit vector $\mathbf{S}_{id}/\|\mathbf{S}_{id}\|$:

$$\mathbf{v}_{Ti} = \left(\mathbf{I} - \frac{\mathbf{S}_{id}\mathbf{S}_{id}^T}{\|\mathbf{S}_{id}\|^2}\right) \tag{15}$$

The original normal vector $\mathbf{S}_{iu}$ is used for boundary integrals and fluxes calculations. Since normal tangency is applied on the deformed normal and the grid is actually not modified, a nonnull normal component results. In this context the wall can be considered as blower/injector according to the direction of the nonnull normal component. Thus the transpiration provides the CFD solver a deflection of its boundaries even if the mesh is actually untouched.

Unsteady simulations require a second term, called *kinematic transpiration* contribution, related to body velocity $\dot{\tilde{\mathbf{x}}}$. The transpiration boundary condition of Eq. (15) for a moving and deforming body becomes

$$\mathbf{v}_{Ti} = \left(\mathbf{I} - \frac{\mathbf{S}_{id}\mathbf{S}_{id}^T}{\|\mathbf{S}_{id}\|^2}\right)\mathbf{v}_i - \frac{\mathbf{S}_{id}\mathbf{S}_{id}^T}{\|\mathbf{S}_{id}\|^2}(\dot{\mathbf{x}}_O + \boldsymbol{\omega}_O \times \mathbf{R}_O\tilde{\mathbf{x}} + \mathbf{R}_O\dot{\tilde{\mathbf{x}}}) \tag{16}$$

The condition of no-flow through the physical boundary is applied again along the deformed normal direction, which depends both on structural deformation and rigid body deflections. This allows to use the transpiration boundary condition to simulate aeroelastic effects for the maneuvered flight.

Figure 3 shows an application of the transpiration boundary condition to account for antisymmetric aileron deflection. The local pressure variation can be appreciated.

V. Spatial Coupling of Nonmatching Discretizations

The stresses on the wet surfaces resulting from aerodynamics are determined as soon as the dynamic state of the moving boundaries is determined. Multidisciplinary problems require proper coupling conditions. For a continuum

$$\left.\boldsymbol{\sigma}_s = -p\,\mathrm{d}\mathbf{S} + \boldsymbol{\sigma}_f \cdot \mathrm{d}\mathbf{S} \qquad \mathbf{x}_s = \mathbf{x}_f \qquad \dot{\mathbf{x}}_s = \dot{\mathbf{x}}_f\right\} \quad \text{on } \Gamma \tag{17}$$

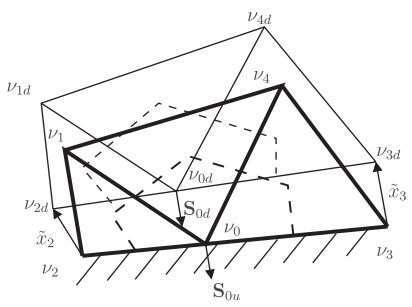

Fig. 2 Normal variation for moving wall boundary.

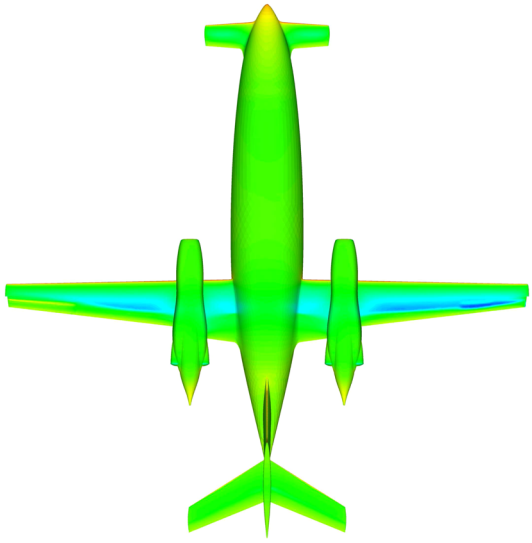

Fig. 3 Piaggio P180, pressure contour, $M_\infty = 0.75$, Euler analysis, ailerons deflection $\delta = 5$ deg (right down, left up).

where subscripts $(\cdot)_s$ and $(\cdot)_f$ respectively indicate the structural and viscous flow domains, $\boldsymbol{\sigma}_s$ is the stress tensor in the structural domain, p is the pressure, and $\boldsymbol{\sigma}_f$ is the deviatoric stress in the viscous flow domain. The first of Eqs. (17) expresses the stress equilibrium on the boundary interface Γ, while the other two are kinematic compatibility conditions; the last needs to be relaxed to normal compatibility for inviscid flows. The two fields are actually solved in weak form. Consequently, a discrete approximation for Eq. (17) must be derived, retaining the conservation properties of the original problem, namely conservation of mass, momentum and work exchanged along Γ. The conservation is trivially retained when the two domains have matching discrete interfaces and compatible approximation spaces. However, in realistic applications, the fluid and structure meshes are not compatible, since they are usually discretized according to spatial resolution requirements typical of each discipline.

Methods referred to as *alternative interpolation* introduce a new set of basis functions that are unrelated to those used in the structural and aerodynamic numerical schemes. To guarantee conservation between the two domains, the correct strategy consists in enforcing the coupling conditions in a weak sense only, through the use of variational principles. The work exchange can be investigated using the PVW [60]. Consider $\delta\mathbf{x}_f$ and $\delta\mathbf{x}_s$ as admissible virtual displacements for the fluid and the structure. "Admissible" means that the traces of the displacement, namely the restriction to the boundary in the appropriate functional space used by each solver, must be equal:

$$\mathrm{Tr}\,(\delta\mathbf{x}_f)|_\Gamma = \mathrm{Tr}(\delta\mathbf{x}_s)|_\Gamma \tag{18}$$

The relationship between the two admissible virtual displacements can be written as

$$(\delta\mathbf{x}_f)_i = \sum_{j=1}^{j_s} h_{ij}(\delta\mathbf{x}_s)_j \tag{19}$$

$\delta\mathbf{x}_{f_i}$ are the discrete values of $\delta\mathbf{x}_f$ on fluid nodes; h_{ij} are the elements of a generic interpolation matrix $\mathbf{H}$. When the shape functions N_i of the aerodynamic field are considered, the virtual displacement is

$$\delta\mathbf{x}_f = \sum_{i=1}^{i_f} N_i \sum_{j=1}^{j_s} h_{ij}(\delta\mathbf{x}_s)_j \tag{20}$$

The virtual work on both sides of the interface is

$$\begin{aligned}\delta W_f &= \int_{\Gamma_f} (\delta\mathbf{x}_s)_j \sum_{j=1}^{j_s} h_{ij} \sum_{i=1}^{i_f} N_i \cdot (-p\mathbf{I} + \boldsymbol{\sigma}_f)\cdot \mathrm{d}\mathbf{S} = \delta W_s \\ &= \sum_{j=1}^{j_s} (\delta\mathbf{x}_s)_j \cdot \mathbf{f}_{s_j}\end{aligned} \tag{21}$$

The nodal loads $\mathbf{f}_{f_i}$ for each CFD boundary grid point

$$\mathbf{f}_{f_i} = \int_{\Gamma_f} \sum_{i=1}^{i_f} N_i \cdot (-p\mathbf{I} + \boldsymbol{\sigma}_f)\cdot \mathrm{d}\mathbf{S} \tag{22}$$

are computed using the correct approximation space used in the CFD solver. Equations (21) and (22) yield

$$\mathbf{f}_{s_j} = \sum_{i=1}^{i_f} h_{ij}\mathbf{f}_{f_i} \tag{23}$$

The loads on the structural nodes, $\mathbf{f}_{s_j}$, result from right-multiplying the fluid loads $\mathbf{f}_{f_i}$ by the transpose of the interface matrix $\mathbf{H}$ that maps the virtual displacements of the two grids, Eq. (19).

The conservation problem is shifted on the definition of the interface matrix $\mathbf{H}$. A conservative interface matrix, enforcing the compatibility of Eq. (18), is built using a weak/variational formulation based on weighted least-squares:

$$\text{Minimize} \int_\Gamma \phi(\mathbf{x})(\mathrm{Tr}(\delta\mathbf{x}_f)|_\Gamma - \mathrm{Tr}(\delta\mathbf{x}_s)|_\Gamma)^2\,\mathrm{d}\mathbf{A} \tag{24}$$

where ϕ is a weight function. The solution should have the additional properties of a) computational efficiency; b) correct smoothness of the resulting surface; c) quality of reproduction. This can be obtained using the moving least-squares technique [61,62]. Given a compact space $\Omega \subseteq \mathbb{R}^n$, the reconstruction of a function $f \in C^d(\Omega)$ from its values $f(\bar{\mathbf{x}}_1), \ldots, f(\bar{\mathbf{x}}_N)$ on scattered distinct points $X_s = \{\bar{\mathbf{x}}_1, \ldots, \bar{\mathbf{x}}_N\}$ is needed. An analytical expression for f is not required; an efficient method to compute the value of f on a different set of centers $X_f = \{\mathbf{x}_1, \ldots, \mathbf{x}_N\}$ suffices. The proposed method uses local approximations of f expressed as the sum of monomial basis functions $p_i(\mathbf{x}) \in \mathbb{P}_d$:

$$\hat{f}(\mathbf{x}) = \sum_{i=1}^{m} p_i(\mathbf{x})a_i(\mathbf{x}) \equiv \mathbf{p}^T(\mathbf{x})\mathbf{a}(\mathbf{x}) \tag{25}$$

where m is the number of basis functions, with coefficients $a_i(\mathbf{x})$. $\mathbb{P}_d \subseteq C^d(\Omega)$ is a finite dimensional space of basis functions; usually it is spanned by polynomials, but other functions can be adopted. The coefficients $\mathbf{a}_i(\mathbf{x})$ are obtained by a weighted least square fit for the approximation $\hat{f}$:

$$\text{Minimize } J(\mathbf{x}) = \int_\Omega \phi(\mathbf{x} - \bar{\mathbf{x}})(\hat{f}(\mathbf{x}, \bar{\mathbf{x}}) - f(\bar{\mathbf{x}}))^2\,\mathrm{d}\Omega(\bar{\mathbf{x}}) \tag{26}$$

with the constraint that the local approximation $\hat{f}$ is expressed in terms of the known position of local centers belonging to X_s as

$$\hat{f}(\mathbf{x}, \bar{\mathbf{x}}) = \sum_{i=1}^{m} p_i(\bar{\mathbf{x}})a_i(\mathbf{x}) \tag{27}$$

The coefficients $a_i(\mathbf{x})$ are computed using Eq. (27) for $\hat{f}$; this is equivalent to Eq. (25) when $\mathbf{x} = \bar{\mathbf{x}}_i$. Consequently, the local approximation $\hat{f}(\mathbf{x})$ exactly recovers data at the known centers $\bar{\mathbf{x}}_i$. Equation (26) is completely equivalent to Eq. (24). The displacements on the fluid grid are represented by function $\hat{f}$.

When the problem is cast in this form, it can be localized by choosing compact-support weight functions, like smooth non-negative radial basis functions (RBFs) [63]. Weight RBF are usually written as $\phi(r/\delta)$, where δ is a scaling factor that changes the function support at different space centers. It allows the user to adapt the support radius to the problem, to ensure that enough points are covered, while points far away have no influence (see Fig. 4b).

VI. Tightly Coupled Solution Procedure

The coupling of the two solvers is called "tight" since they iterate during convergence at each time step. The coupling algorithm is

1) The MSD solver predicts the configuration ($\mathbf{x}_O$, $\mathbf{R}_O$, $\mathbf{u}$ and their time derivatives) at a new time step.

2) The MSD solver sends the predicted configuration to the CFD solver.

3) The CFD solver computes the aerodynamic loads based on the geometry received from the MSD solver.

4) The CFD solver sends the aerodynamic loads to the MSD solver.

5) The MSD solver uses the aerodynamic loads received from the CFD solver to compute the updated solution for the current iteration.

6) The MSD solver sends the updated geometry to the CFD solver.

7) The loop goes back to point (3).

When the CFD solver converges, it stops waiting for updated geometry information and prepares for the subsequent time step; the MSD solver iterates until convergence using the last set of air loads. Variants of this scheme consist in performing subiterations between each communication phase.

In the current implementation, information exchange between the MSD and the CFD solvers consists of 1) the linear and angular velocity, $\dot{\mathbf{x}}_O$ and $\boldsymbol{\omega}_O$, and the orientation matrix, $\mathbf{R}_O$, of the reference

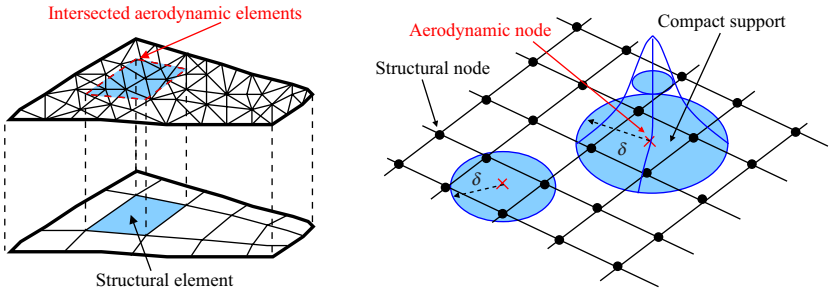

a) Non-matching element meshes **b) Interpolation on scattered nodes**

Fig. 4 Different interpolation strategies along boundary interfaces.

rigid body motion of the CMS element and 2) the value of the modal variables, $\mathbf{u}$, and their time derivative, $\dot{\mathbf{u}}$.

The CFD solver takes care of mapping the motion described by the CMS element kinematics into the appropriate boundary conditions for the CFD analysis.

The information exchange between CFD and MSD solvers consists of 1) the overall force and moment applied to the rigid body dynamics equations of the CMS element and 2) the generalized forces that apply to the generalized dynamics equations of the CMS element.

The CFD solver takes care of computing the overall forces and moments and the generalized forces from the pressure distribution.

From the MSD standpoint, the interface is general; in the current implementation, communication occurs through textual files. An analogous communication layer based on UNIX sockets is available as well. A native exchange format in textual/binary form, and a format specifically designed to interoperate with Edge's file primitives have been designed and implemented. Right now the cost of interprocess communication is not considered critical, since the amount of information exchanged is quite limited. The computational cost of the MSD analysis is a minimal fraction of that of the CFD analysis. As a consequence, the serialization of MSD and CFD interaction does not appear to be an issue.

An analogous interface has been designed to exchange information at the node level, to allow the direct coupling of CFD with nonlinear FE structural models. This approach has not been addressed yet.

The coupling illustrated in this work has been released in MBDyn 1.3.5, January 2009, and will be part of the imminent release 5.1 of Edge.

VII. Flutter of the AGARD 445.6 Benchmark

The procedure is validated using the AGARD 445.6 weakened wing, a well-known three-dimensional standard aeroelastic configuration tested in the transonic wind-tunnel at NASA Langley. The semispan wind-tunnel model of the wing is made of laminated mahogany, with NACA 65A004 airfoil, a quarter-chord sweep angle of 45 deg, an aspect ratio of 1.65 and a taper ratio of 0.66. To reduce the stiffness, the wing was weakened by holes drilled through it and filled with foam. The weakened model number three is considered because all flow conditions (sub, trans- and supersonic) were tested. Further information about models, test setups and conditions are reported in Yates [64].

The structural model consists of the first four undamped normal modes. The first two, respectively identified as first bending and first torsional, are primarily involved in flutter. Figure 5 shows the computational domain used for Euler calculations with 1,066,361 tetrahedral elements and 227,278 nodes. Considering the relatively simple model, without control surfaces, the mesh-deformation capabilities of the flow solver are exploited. The MSD model consists of a grounded CMS element. Vibration modes in clamped condition, determined during the experimental survey, are used to model structural flexibility. Modal frequencies are 9.60, 38.17, 48.35, and 91.55 Hz.

The experimental flutter point at the subsonic flight regime $M_\infty = 0.678$ is assessed by means of the coupled MSD/CFD model. A harmonic excitation is given at the trailing edge of the tip, and the stability of the system is assessed by examining the response. The airfoil is symmetric; zero angle of attack is considered as reference. As a consequence, trim is straightforward. Experimental flutter occurs at a flight speed of 231.37 m/s, with a dynamic pressure of 4710 Pa. In these flight conditions, the numerical model experiences undamped oscillations, as depicted in Figs. 6a and 6b. At a lower dynamic pressure of 3327 Pa, for the same Mach number, smaller unsteady generalized aerodynamic forces result. The system is stable, as indicated by the significantly damped oscillations illustrated in Figs. 6c and 6d.

VIII. Piaggio P180 Model

In the current study, an experimental modal model, obtained from GVT, is used to represent the structure of the Piaggio P180 in unconstrained conditions. Using the modal appropriation technique (Ewins [65]), the first 39 deformable modes were identified in terms of mode shape, generalized mass, frequency and damping. The experiment measured the free-free modes of the airframe suspended by very soft elastic suspensions. A total of 159 uniaxial

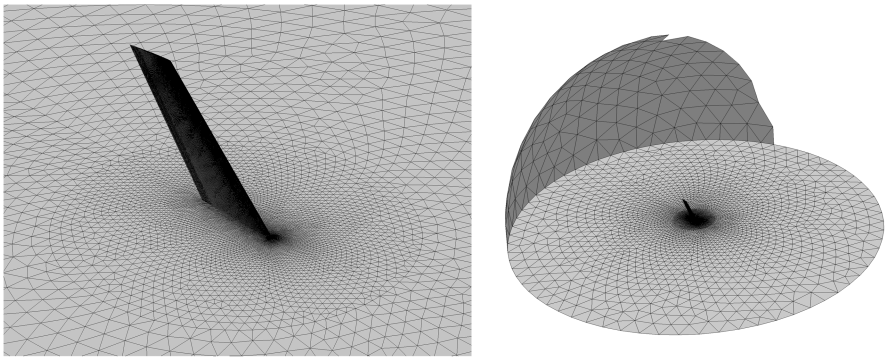

a) Mesh detail **b) Volume mesh**

Fig. 5 Computational domain for the AGARD 445.6 wing.

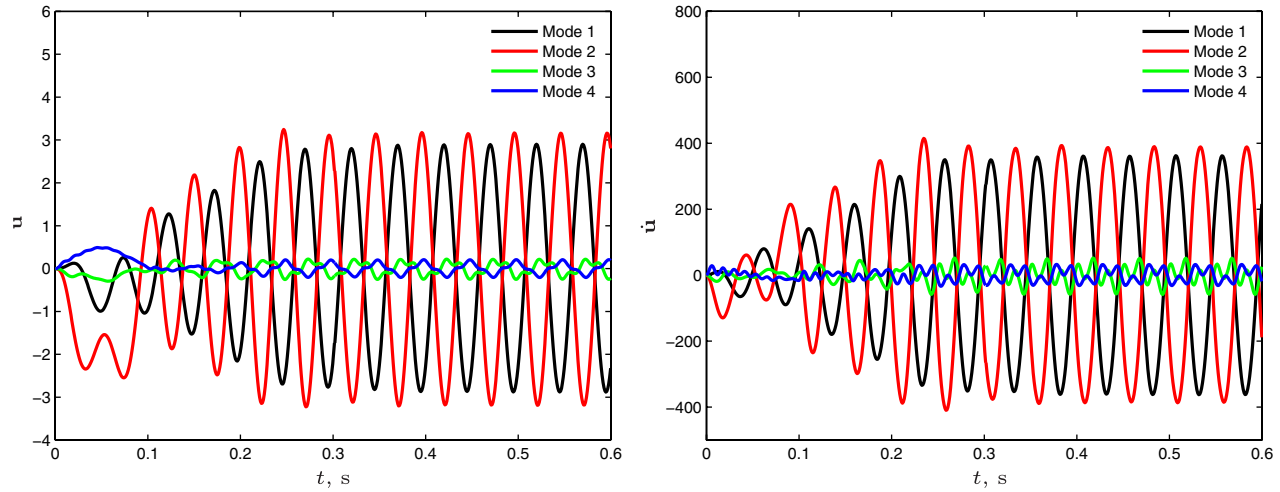

a) Undamped, modal amplitudes

b) Undamped, modal velocities

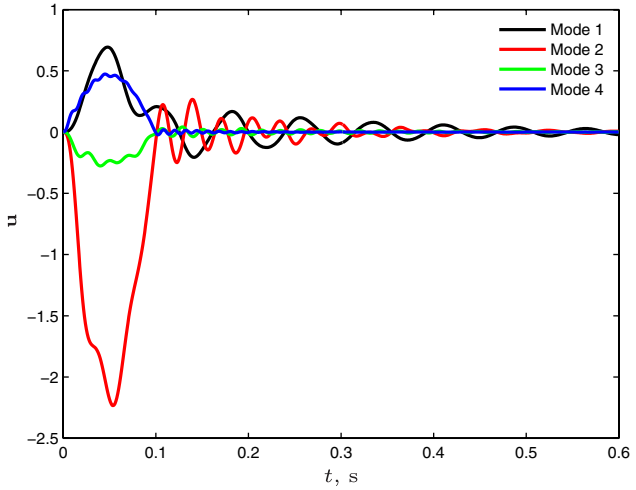

c) Damped, modal amplitudes

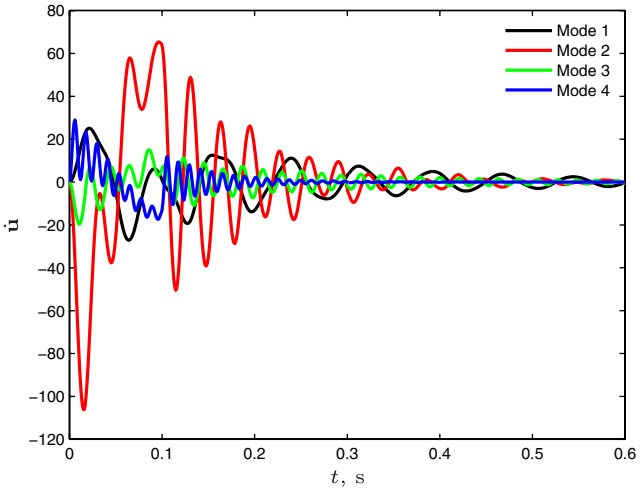

d) Damped, modal velocities

Fig. 6 Application for the AGARD 445.6 wing, undamped (above) and damped (below) response.

accelerometers were applied on aerodynamic surfaces, nacelles and fuselage. Their orientation was determined to allow to measure accelerations normal to lifting surfaces. Displacements along those directions are essential to characterize mode shapes for aeroelasticity.

However, the available measures provide an incomplete displacement field, since only some components of the motion were measured. Thus, shape functions present discontinuities. Particularly problematic are those along the lines of intersection of the different surfaces. This may be troublesome in CFD computations, since the use of an incomplete displacement field leads to surface clashing, and hence mesh invalidation, because of negative volumes and highly distorted cells. When aeroelastic analysis is based on aerodynamic potential methods, normal displacements directly concur to the definition of aerodynamic loads. This is also the case when transpiration boundary conditions are applied to CFD analysis, since only normal displacement contributions are taken into account, while the mesh is not updated according to the deformed shape.

To solve the incompatibility problem, a reconstruction of the whole displacement field from separate components available on the different items is required. To improve this process, and significantly the smoothness of the reconstruction, several intermediate nodes are added to the original grid of accelerometers based on engineering judgment. The motion of added points is heuristically interpolated from the available measures using least squares.

Figure 7 shows the CFD mesh used for Euler calculations. The complete aircraft is modeled using 1,426,946 tetrahedral cells with 298,523 nodes. Figure 8 shows the application of the spatial coupling method to recover the displacements of the CFD boundaries according to different mode shapes on the structural mesh. The coupling is only applied to the structural velocities in the applications presented in this work to impose transpiration boundary conditions without actually deforming the aerodynamic mesh.

The solution of the trim problem is iteratively sought in a manner similar to an experimental wind-tunnel survey, as outlined in Fig. 9. The model is pinned along its principal pitch axis. A revolute hinge allows a relative rotation ψ with respect to the flow field, thus changing the angle of attack. A deflection of the elevator δ_e is used to impose vertical force and pitch moment equilibrium. The absolute path of the aircraft is imposed to be horizontal with respect to the ground (absolute reference frame) and gravity is assumed to act along absolute vertical axes. The aircraft is considered trimmed when the vertical reaction force vanishes. The effect of thrust on the trim configuration is neglected; as a consequence a nonnull horizontal reaction appears. When the aircraft rotates about the revolute hinge, the new velocity $\dot{\mathbf{x}}_O^{(n)}$ of the body in the moving reference frame is passed to the CFD solver, which converts it into nodal mesh velocities as if the aircraft were moving with respect to still air and ground. A dummy elevator mode is added, consisting in unit rigid elevator rotation. Structural displacements and elevator deflection are accounted for in the same manner through the transpiration boundary condition. An approach similar to that proposed by Raveh et al. [66] is carried out. As outlined in Fig. 10, the iterative process is made of three different nested iteration levels:

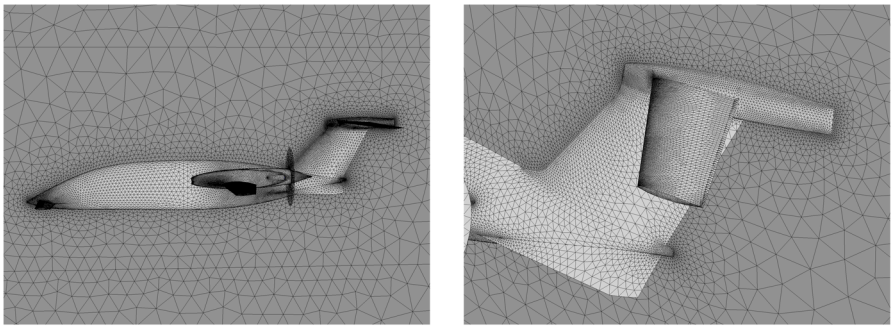

a) Element growth b) T-tail detail

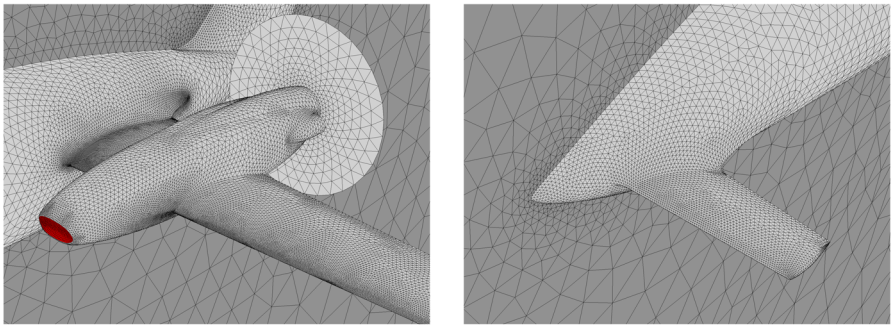

c) Nacelle detail d) Canard detail

Fig. 7 CFD mesh used for the aeroelastic analysis of the P180.

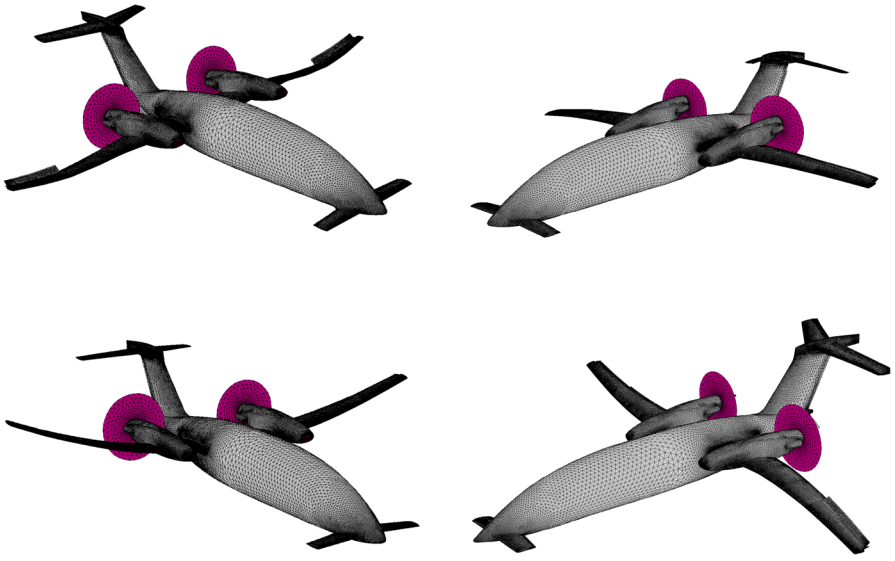

Fig. 8 Application of spatial coupling method for different modal shapes.

1) At the basic level, the CFD and CSM iteratively solve their own subset of equations until convergence on flow and mechanical variables.

2) At the intermediate level, part of the coupling process outlined in Sec. VI is carried out, staggering the update of reference and elastic coordinates.

3) The outermost level simply indicates the kth trim iteration; it is executed until overall convergence of reference and elastic coordinates.

At midlevel (2), the deformed trim shape for the current configuration is computed while freezing variables $\dot{\tilde{\mathbf{x}}}_O^{(n)}$ and $\boldsymbol{\delta}^{(n)}$ that describe the motion of the aircraft in the body-reference frame and its controls. A fixed-point iteration

$$\mathbf{K}_{\mathbf{uu}}\mathbf{u}^{(i+1)} = \mathbf{f}_{\mathbf{u}}^{a}(\mathbf{u}^{(i)}, \dot{\tilde{\mathbf{x}}}_O^{(n)}, \boldsymbol{\delta}^{(n)}) \tag{28}$$

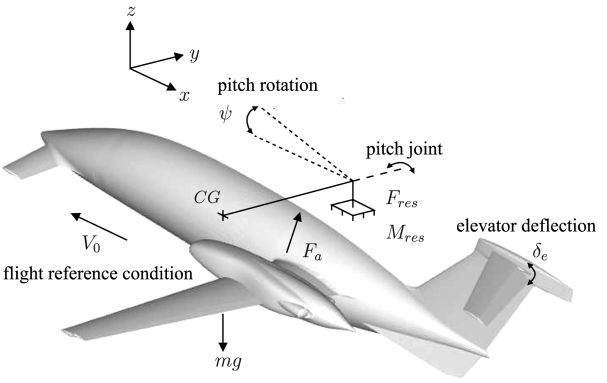

Fig. 9 Sketch of the numeric experiment.

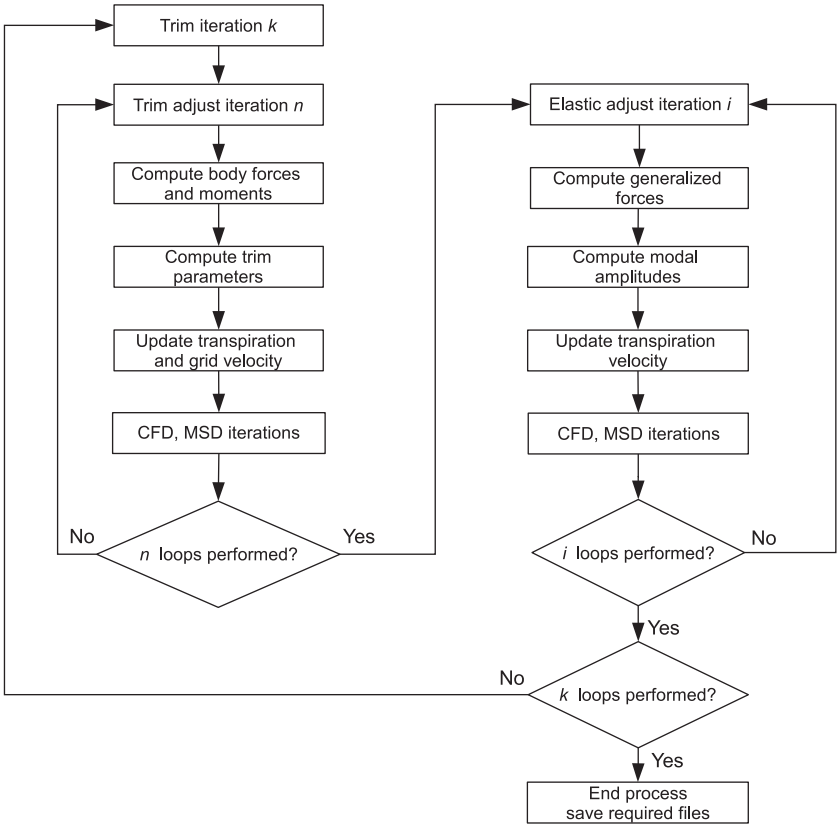

Fig. 10 Flow chart of the deformable trim process.

is used until equilibrium between elastic and aerodynamic forces dependent on the assumed structural configuration is found. To avoid excessive overshoots, relaxation is usually introduced.

Inertia relief is implicitly included when generalized aerodynamic forced are determined, since the $\mathbf{\Psi}$ are mean axes shapes. The approach of Eq. (28) neglects $\partial \mathbf{f}_{\mathbf{u}}^{a} / \partial \mathbf{u} = -\mathbf{K}_{\mathbf{uu}}^{a}$, the Jacobian matrix of the generalized aerodynamic forces with respect to the elastic coordinates, commonly referred to as the aerodynamic stiffness matrix, implicitly assuming that the structural configuration is well below static aeroelastic divergence, namely $\mathbf{K}_{\mathbf{uu}} + \mathbf{K}_{\mathbf{uu}}^{a} > 0$.

As soon as the iteration convergences, a maneuver trim loop adjusts controls and aircraft attitude to obtain the static equilibrium position. In this simple case, a dummy discrete feedforward controller is set up in the MSD solver, based on a linearization of rigid body aerodynamic forces and moments. Corrections to elevator deflection δ_e and aircraft joint pitch angle ψ are determined as

$$\mathbf{x}^{(n+1)} = \mathbf{x}^{(n)} + (\mathbf{J}_{\mathbf{x}}^{a})^{-1} \Delta \mathbf{f}(\mathbf{u}^{(i)}, \mathbf{x}^{(n)}) \tag{29}$$

where $\mathbf{x} = (\psi, \delta_e)^T$, while $\mathbf{J}_{\mathbf{x}}^{a}$ contains an estimate of the derivatives of the aerodynamic vertical force and pitch moment with respect to pitch and elevator deflection. They may be known from experiments, or be evaluated using the CFD solver.

Since aerodynamic loads are nonlinear, a sampling campaign is needed to determine a database for each configuration point, usually based on computationally expensive finite differences. The inclusion of aeroelastic effects on these derivatives, using the CFD solver, leads to additional computational cost. As a consequence, for this simple

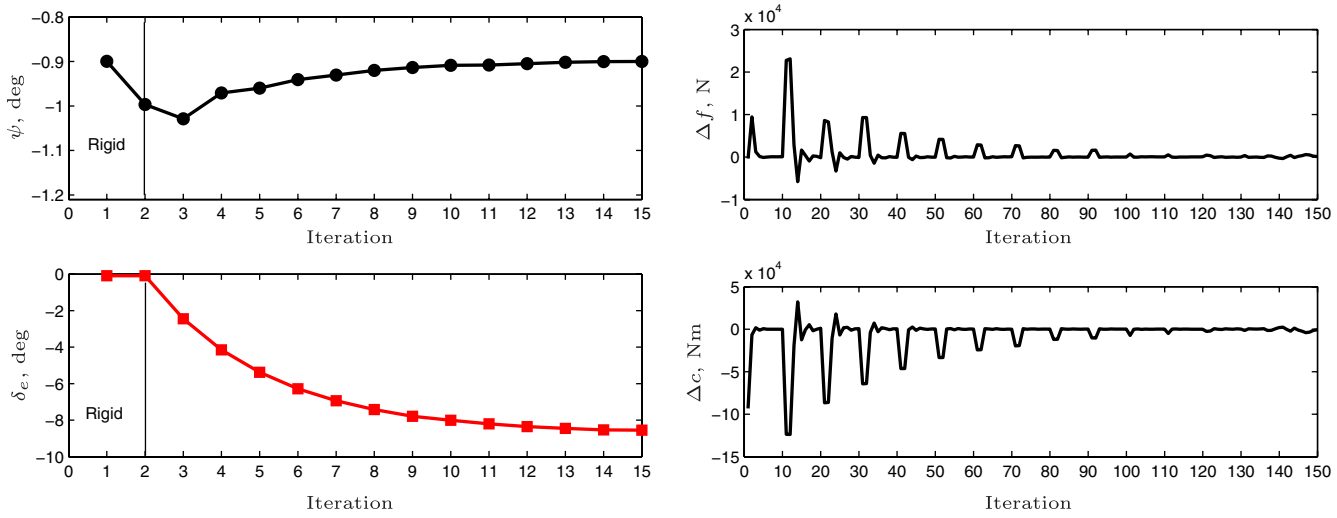

a) Trim variables at each iteration **b) Residual on forces and moments**

Fig. 11 Convergence of the trim problem.

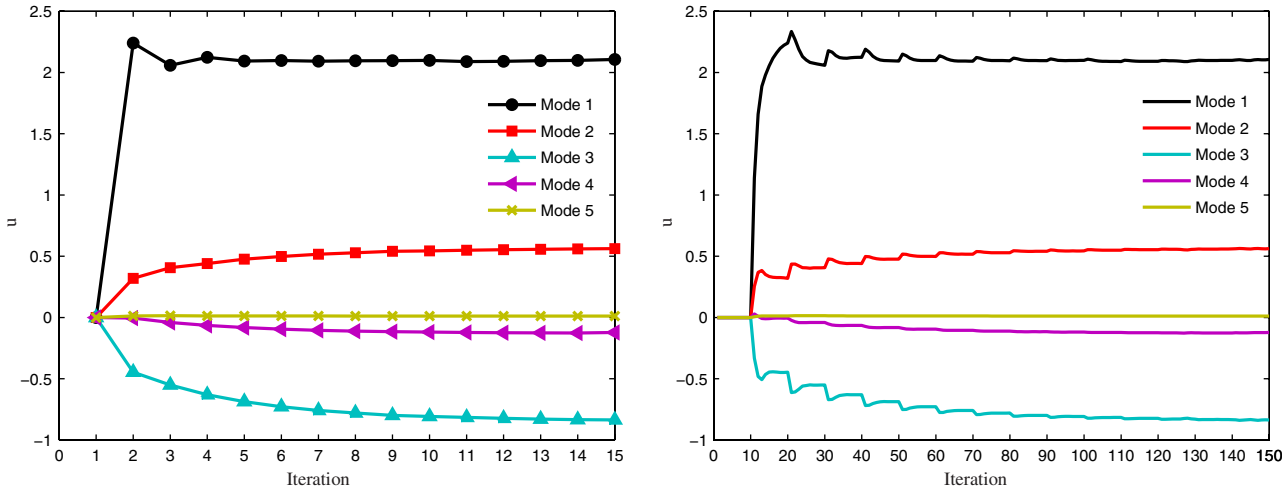

a) Values at each trim step iteration b) Values during sub-cycling

Fig. 12 Modal amplitudes history.

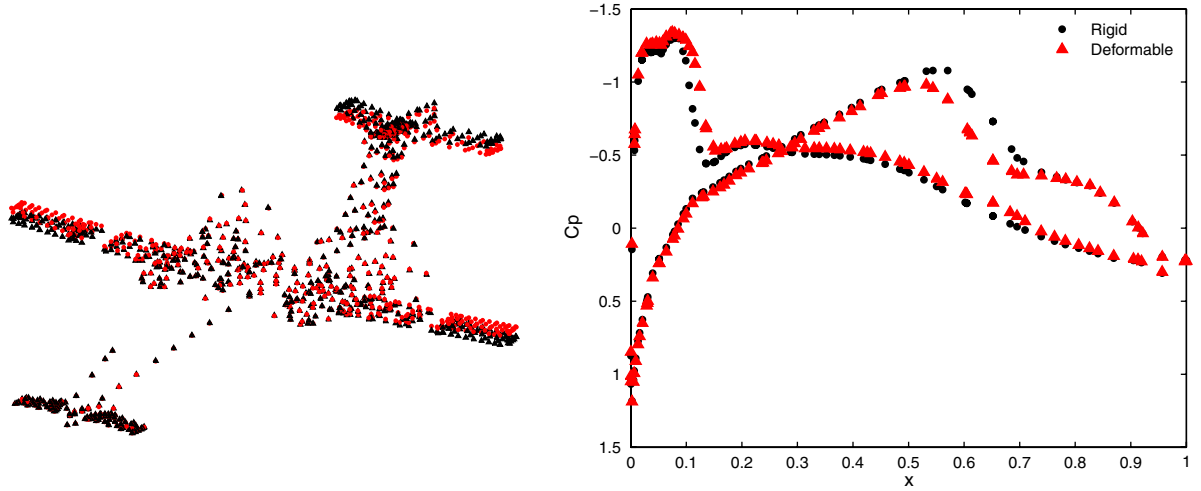

a)Initial (triangles) and final deformed shape (circles) b) Pressure distribution, 88% span

Fig. 13 Results of the deformable trim process.

application $\mathbf{J}_{\mathbf{x}}^{a}$ is never updated. It is defined once and for all starting from the undeformed reference condition of null pitch and elevator deflection. This destroys the theoretical superlinear convergence of Eq. (29). Nevertheless, the approximation is acceptable when structural deflections are small and a good guess is used as starting point.

One hundred explicit iterations for the CFD solver are used at level (1); 10 steps are used to update both reference and elastic coordinates for the two iterative loops at midlevel (2). Consequently, each trim iteration requires 2000 explicit iterations of the CFD solver. Figure 11a reports the angle of attack ψ and the elevator deflection δ_e at the trim iterations. A guess value is given at the first step; in one

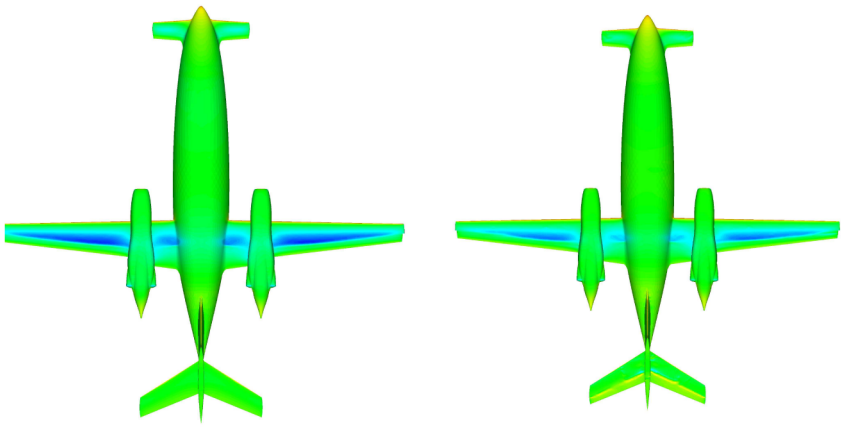

a) Rigid trim b) Deformable trim

Fig. 14 Pressure distribution at trim configuration.

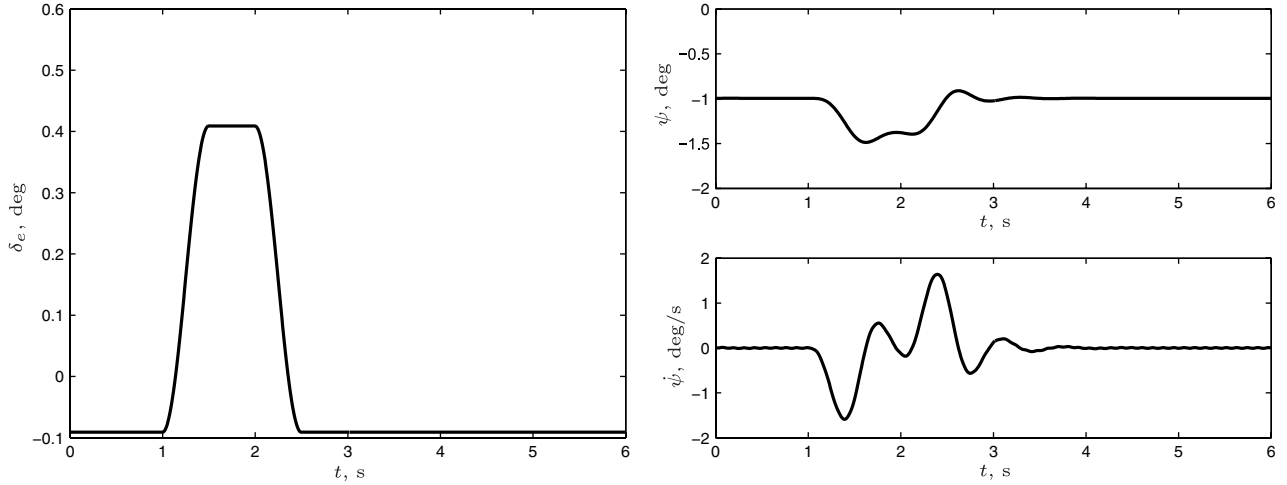

a) Elevator deflection **b) Pitch rotation and rate**

Fig. 15 Input and response for the pinned case.

iteration the trim solution for the rigid aircraft is essentially determined; elastic iterations follow. Figure 11b shows the residual of vertical force and pitch moment acting on the pitch hinge within each trim iteration. As mentioned earlier, 10 adjustments are allowed within each trim iteration. After approximately eight global iterations the procedure converges. Figure 12a summarizes the value of modal amplitudes at each elastic trim iteration. Figure 12b reports modal amplitudes at each inner adjustment. It shows that, apart from the first step, 10 iterations for elastic updating are more than enough, since convergence is indeed reached much earlier.

The difference between rigid and flexible trim solutions is clear: in the selected configuration, the angle of attack required by the rigid model is negative, and the deflection of the elevator is approximately null. When the aeroelastic trim is considered, a higher angle of attack

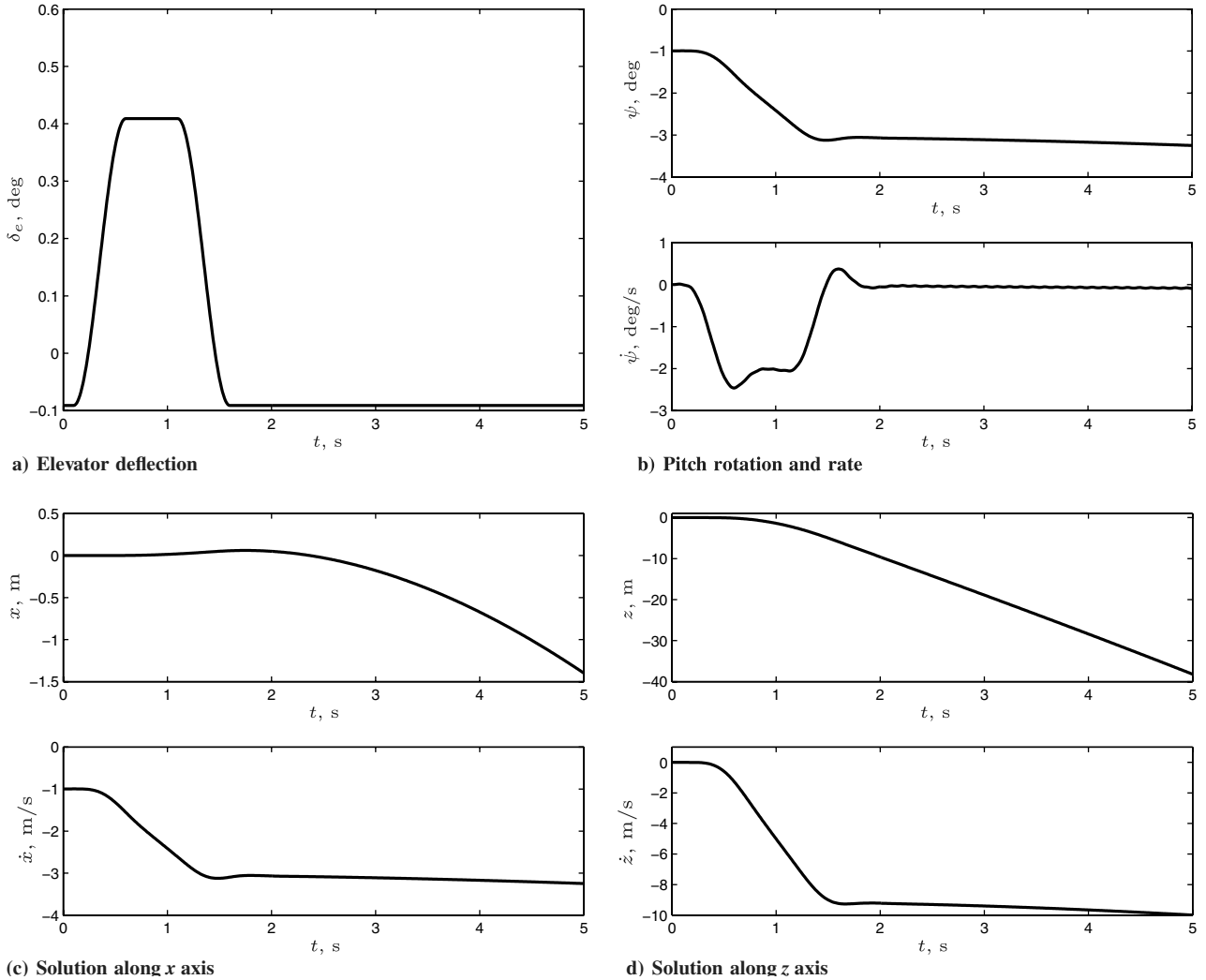

a) Elevator deflection **b) Pitch rotation and rate**

(c) Solution along *x* axis **d) Solution along *z* axis**

Fig. 16 Input and responses for the free flying case.

is required to balance the negative torsional twist of the wing that locally reduces the angle of attack. To counter-balance the pitching aerodynamic moment, the elevator needs to be deflected upward in order to generate negative downlift. The final deformed shape is shown in Fig. 13a, where wing surfaces bend upward, while tail empennages bend downward. Figure 13b shows the difference in chordwise pressure distribution for rigid and deformable trim configurations. The intensity of the shock reduces, and its position moves upflow. Figure 14 shows the difference of pressure distribution at 88% of the span for the rigid and deformable cases at trim cruise flight. The change in pressure distribution along the stabilizer required by the deformable trim is clear as well.

IX. Response to Control Input

The coupled procedure has been applied to the analysis of the P180 aircraft during trim and transient flight conditions. To reduce the complexity of the problem, a symmetric flight condition has been considered. The reference flight condition is $M_\infty = 0.75$ at sea level. The real aircraft cannot operate in this flight condition, but it may be representative of flutter clearance analysis. It was designed to ensure a developed shock wave on the wings.

An incrementally complex problem has been considered:

1) The aircraft is trimmed in level flight computing the required pitch and elevator settings (Sec. VIII).

2) An elevator motion is prescribed, starting from the trimmed flight condition, with the aircraft constrained by a revolute joint about the pitch axis.

3) The same elevator motion is prescribed, with the aircraft constrained only by symmetry constraints (vertical and longitudinal displacement, pitch rotation allowed); the thrust resulting from the trim analysis is added using a "follower" force.

The prescribed elevator motion consists in a sequence of two opposite smoothed steps, illustrated in Fig. 15a. The model constrained by a revolute hinge about the pitch axis responds with the pitch motion of Fig. 15b. The initial pitch is completely recovered when the control input returns to zero. This analysis shows the stability of the 'short period' (pitch) motion of the model.

The free model, on the contrary, ends up in an almost steady descent, as illustrated by Figs. 16b–16d. The motion of the aircraft should evolve into a phugoid transient (altitude/longitudinal speed oscillation). However, its period is much longer than this analysis is expected to capture. From an aeroelastician's point of view, such a long period would allow to analyze the phugoid problem using quasi-steady, or even steady approximations of the aerodynamic loads, instead of the unsteady CFD analysis considered in this work.

X. Conclusions

The paper presents the tightly coupled CFD and MSD analysis of the aeroelastic behavior of a transonic aircraft. This type of problem requires the use of sophisticated fluid dynamics models to capture the relevant dynamic effects of unsteady transonic flow, including aerodynamic loads that depend on unsteady compressibility effects. The use of MSD provides the capability to consider nonlinear flight mechanics equations of motion. It also allows to introduce structural flexibility; in the proposed case, CMS of the structure, based on normal vibration modes, is considered.

The work-preserving coupling algorithm between the fluid and the structure is illustrated. The efficiency of the CFD solver (FOI's Edge) and the versatility of the MSD solver (MBDyn) allowed to implement a tight coupling procedure. As a consequence, the structural and the fluid dynamics problems are solved simultaneously, exchanging boundary conditions at each iteration of an implicit nonlinear solution procedure.

The results of trim and transient analysis applied to realistic aerodynamic and structural models of the aircraft show the soundness of the proposed procedure. This preliminary development phase of the coupling did not significantly focus on efficiency. In fact, the CFD solver was mostly run on a single-CPU, with the MSD solver running on a separate CPU of a multicore computer. Nonetheless, realistic discretizations of the CFD problem could be analyzed during transients in relatively short wall-clock times. The foreseen availability of a parallel implementation of the CFD solver promises significantly reduced simulation times.

Acknowledgments

The authors acknowledge Piaggio Aero Industries S.p.A. for authorizing the application of the proposed procedure to the P180 aircraft, and FOI for providing access to the Edge solver.

References

[1] Patil, M. J., and Hodges, D. H., "Flight Dynamics of Highly Flexible Flying Wings," *Journal of Aircraft*, Vol. 43, No. 6, 2006, pp. 1790–1798.
doi:10.2514/1.17640

[2] Ashley, H., "Observations on the Dynamic Behavior of Large Flexible Bodies in Orbit," *AIAA Journal*, Vol. 5, No. 3, March 1967, pp. 460–469.
doi:10.2514/3.4002

[3] Milne, R. D., "Dynamics of the Deformable Aeroplane," British Aeronautical Research Council, TR R&M 3345, 1964.

[4] Milne, R. D., "Some Remarks on the Dynamics of Deformable Bodies," *AIAA Journal*, Vol. 6, No. 3, 1968, pp. 556–5582.
doi:10.2514/3.4541

[5] Meirovitch, L., *Introduction to Dynamics and Control*, Wiley, New York, 1985.

[6] Etkin, B., *Dynamics of Atmospheric Flight*, Wiley, New York, 1972.

[7] Buttrill, C. S., Zeiler, T. A., and Arbuckle, P. D., "Nonlinear Simulation of a Flexible Aircraft in Maneuvering Flight," *Proceedings of the AIAA Flight Technologies Conference*, Aug. 1987, pp. 122–133; also AIAA Paper 87-2501.

[8] Waszak, M. R., and Schmidt, D. K., "Flight Dynamics of Aeroelastic Vehicles," *Journal of Aircraft*, Vol. 25, No. 6, June 1988, pp. 563–571.
doi:10.2514/3.45623

[9] Schmidt, D. K., and Raney, D. L., "Hybrid State Equations of Motion for Flexible Bodies in Terms of Quasi-Coordinates," *Journal of Guidance, Control, and Dynamics*, Vol. 24, No. 3, May–June 2001, pp. 539–546.
doi:10.2514/2.4744

[10] Rodden, W. P., and Love, J. R., "Equation of Motion of a Quasisteady Flight Vehicle Utilizing Restrained Static Aeroelastic Characteristics," *Journal of Aircraft*, Vol. 22, No. 9, 1985, pp. 802–809.
doi:10.2514/3.45205

[11] Bianchin, M., Quaranta, G., and Mantegazza, P., "State Space Reduced Order Models for the Static Aeroelasticity and Flight Mechanics of Flexible Aircraft," *Proceedings of the 17th Congresso Nazionale AIDAA*, AIDAA, Rome, 15–19 Sept. 2003.

[12] Baldelli, D., Chen, P. C., and Panza, J., "Unified Aeroelastic and Flight Dynamic Formulation via Rational Function Approximation," *Journal of Aircraft*, Vol. 43, No. 3, 2006, pp. 763–772.
doi:10.2514/1.16620

[13] Meijer, J. J., and Zwaan, R. J., "Calculation of Frequency Response Functions for Flexible Aircraft," MLR TR 75147 U, 1975.

[14] Raveh, D., "Maneuver Load Analysis of Overdetermined Trim Systems," *Journal of Aircraft*, Vol. 45, No. 1, 2008, pp. 119–129.
doi:10.2514/1.29118

[15] Farhat, C., Pierson, K., and Degand, C., "Multidisciplinary Simulation of the Maneuvering of an Aircraft," *Engineering with Computers*, Vol. 17, No. 1, 2001, pp. 16–27.
doi:10.1007/PL00007193

[16] Raveh, D., "CFD-Based Gust Response Analysis of Free Elastic Aircraft," *Journal of Aeroelasticity and Structural Dynamics*, Vol. 2, No. 1, 2010, pp. 23–34.

[17] Love, M., De La Garza, T., Charlton, E., and Egle, D., "Computational Aeroelasticity in High Performance Aircraft Flight Loads," *Proceedings of the 21st ICAS Congress*, Harrogate, England, U.K., 27 Aug.–1 Sept. 2000.

[18] Fornasier, L., Rieger, H., Tremel, U., and van der Weide, U., "Time-Dependent Aeroelastic Simulation of Rapid Maneuvering Aircraft," 40th AIAA Aerospace Sciences Meeting and Exhibit, AIAA Paper 2002-0949, Reno, NV, 14–17 Jan. 2002.

[19] Schütte, A., Einarsson, G., Raichle, A., Schöning, B., Mönnich, W., Orlt, M., Neumann, J., Arnold, J., and Forkert, T., "Numerical Simulation of Maneuvering Aircraft by Aerodynamic, Flight-Mechanics, and Structural-Mechanics Coupling," *Journal of Aircraft*, Vol. 46, No. 1, 2009, pp. 53–64.

doi:10.2514/1.31182
[20] Masarati, P., Piatak, D. J., Quaranta, G., and Singleton, J. D., "Further Results of Soft-Inplane Tiltrotor Aeromechanics Investigation Using Two Multibody Analyses," American Helicopter Society 60th Annual Forum, Baltimore, MD, 7–10 June 2004.
[21] Spieck, M., Krüger, W., and Arnold, J., "Multibody Simulation of the Free-Flying Elastic Aircraft," 46th AIAA/ASME/ASCE/AHS/ASC Structures, Structural Dynamics, and Materials Conference, AIAA Paper 2005-2280, Austin, TX, 18–21 April 2005.
[22] Krüger, W., and Spieck, M., "Aeroelastic Effects in Multibody Dynamics," *Vehicle System Dynamics*, Vol. 41, No. 5, 2004, pp. 383–399.
[23] Schiehlen, W., "Multibody System Dynamics: Roots and Perspectives," *Multibody System Dynamics*, Vol. 1, No. 2, June 1997, pp. 149–188. doi:10.1023/A:1009745432698
[24] Shabana, A. A., "Flexible Multibody Dynamics: Review of Past and Recent Developments," *Multibody System Dynamics*, Vol. 1, No. 2, June 1997, pp. 189–222. doi:10.1023/A:1009773505418
[25] Zaki, A., Reveles, N., Smith, M. J., and Bauchau, O. A., "Using Tightly-Coupled CFD/CSD Simulation for Rotorcraft Stability Analysis," 66th AHS Forum, Phoenix, AZ, 11–13 May 2010.
[26] Yeo, H., Potsdam, M., and Ormiston, R. A., "Application of CFD/CSD to Rotor Aeroelastic Stability in Forward Flight," 66th AHS Forum, Phoenix, AZ, 11–13 May 2010.
[27] Agrawal, O. P., and Shabana, A. A., "Application of Deformable-Body Mean Axis to Flexible Multibody System Dynamics," *Computer Methods in Applied Mechanics and Engineering*, Vol. 56, No. 2, 1986, pp. 217–245. doi:10.1016/0045-7825(86)90120-9
[28] Canavin, J. R., and Likins, P. W., "Floating Reference Frames for Flexible Spacecraft," *Journal of Spacecraft and Rockets*, Vol. 14, No. 12, 1977, pp. 724–732. doi:10.2514/3.57256
[29] Wallrapp, O., and Wiedemann, S., "Simulation of Deployment of a Flexible Solar Array," *Multibody System Dynamics*, Vol. 7, No. 1, 2002, pp. 101–125. doi:10.1023/A:1015295720991
[30] Wallrapp, O., and Wiedemann, S., "Comparison of Results in Flexible Multibody Dynamics Using Various Approaches," *Nonlinear Dynamics*, Vol. 34, Nos. 1–2, 2003, pp. 189–206. doi:10.1023/B:NODY.0000014559.74006.fb
[31] Schwertassek, R., Wallrapp, O., and Shabana, A. A., "Flexible Multibody Simulation and Choice of Shape Functions," *Nonlinear Dynamics*, Vol. 20, No. 4, 1999, pp. 361–380. doi:10.1023/A:1008314826838
[32] Ghiringhelli, G. L., Masarati, P., and Mantegazza, P., "A Multi-Body Implementation of Finite Volume Beams," *AIAA Journal*, Vol. 38, No. 1, Jan. 2000, pp. 131–138. doi:10.2514/2.933
[33] McDaniel, D. R., Cummings, R. M., Bergeron, K., Morton, S. A., and Dean, J. P., "Comparisons of Computational Fluid Dynamics Solutions of Static and Maneuvring Fighter Aircraft with Flight Test Data," *Proceedings of the I MECH E Part G Journal of Aerospace Engineering*, Vol. 223, No. 4, 2009, pp. 323–340. doi:10.1243/09544100JAERO411
[34] Bendiksen, O. O., "Transonic Limit Cycle Flutter/LCO," 45th AIAA/ASME/ASCE/AHS/ASC Structures, Structural Dynamics and Materials Conference, Palm Springs, CA, AIAA Paper 2004-1694, 19–22 April 2004.
[35] Anon., "Certification Specifications for Large Aeroplanes CS25: Amendment 8," European Aviation Safety Agency TR-CS25, 18 Dec. 2009, Annex to ED Decision 2009/017/R.
[36] Cunningham, A. M., "Buzz, Buffet, LCO on Military Aircraft: The Aeroelastician's Nightmares," International Forum on Aeroelasticity and Structural Dynamics (IFASD), Amsterdam, 4–6 June 2003.
[37] Silva, R., Mello, O., and Azevedo, J., "Navier–Stokes-Based Study into Linearity in Transonic Flow for Flutter Analysis," *Journal of Aircraft*, Vol. 40, No. 5, 2003, pp. 997–1000. doi:10.2514/2.6886
[38] Land, N., and Fox, A., "An Experimental Investigation of the Effects of Mach Number, Stabilizer Dihedral and Fin Torsional Stiffness on the Transonic Flutter Characteristics of a Tee-Tail," NASA, TN D–924, 1961.
[39] Jennings, W., and Berry, M., "Effect of Stabilizer Dihedral and Static Lift on *T*-Tail Flutter," *Journal of Aircraft*, Vol. 14, No. 4, 1977, pp. 364–367. doi:10.2514/3.58785
[40] Cavagna, L., Quaranta, G., and Mantegazza, P., "Application of Navier–Stokes Simulations for Aeroelastic Assessment in Transonic Regime," *Computers and Structures*, Vol. 85, Nos. 11–14, 2007, pp. 818–832. doi:10.1016/j.compstruc.2007.01.005, Fourth MIT Conference on Computational Fluid and Solid Mechanics.
[41] Eliasson, P., and Weinerfelt, P., "Recent Applications of the Flow Solver Edge," Seventh Asian CFD Conference, Bangalore, India, 26–30 Nov. 2007.
[42] Donea, J., and Huerta, A., *Finite Element Methods for Flow Problems*, Wiley, New York, 2003.
[43] Fisher, C., and Arena, A., "On the Transpiration Method for Efficient Aeroelastic Analysis Using an Euler Solver," *Proceedings of the AIAA Atmospheric Flight Mechanics Conference*, San Diego, CA, 29–31 July 1996.
[44] Hairer, E., and Wanner, G., *Solving Ordinary Differential Equations*, Vol. 2, 2nd rev. ed., Springer–Verlag, Berlin, 1996.
[45] Wallrapp, O., "Standardization of Flexible Body Modeling in Multibody System Codes, Part 1: Definition of Standard Input Data," *Mechanics of Structures and Machines*, Vol. 22, No. 3, 1994, pp. 283–304. doi:10.1080/08905459408905214
[46] Wallrapp, O., "Flexible Bodies in Multibody System Codes," *Vehicle System Dynamics*, Vol. 30, Nos. 3–4, 1998, pp. 237–256. doi:10.1080/00423119808969450
[47] Forsberg, K., Gledhill, I. M. A., Eliasson, P., and Nordström, J., "Investigation of Acceleration Effects on Missile Aerodynamics Using CFD," *Proceedings of the 21st Applied Aerodynamics Conference*, Orlando, FL, 6–16 June 2003.
[48] Girodroux-Lavigne, P., Guillemot, S., Henshaw, M., Karlsson, A., Selmin, V., Smith, J., Teupootahiti, E., and Winzell, B., "Comparison of Static and Dynamic Fluid-Structure Interaction Solutions in the Case of a Highly Flexible Modern Transport Aircraft Wing," *Aerospace Science and Technology*, Vol. 7, No. 2, 2003, pp. 121–133. doi:10.1016/S1270-9638(02)00007-X
[49] Peng, S.-H., "Hybrid RANS-LES Modelling Based on Zero- and One-Equation Models for Turbulent Flow Simulation," *Proceedings of 4th International Symposium Turbulence and Shear Flow Phenomena*, Vol. 3, 2005, pp. 1159–1164.
[50] Amoignon, O., Pralits, J., Hanifi, A., M., B., and Henningson, D., "Shape Optimization for Delay of Laminar-Turbulent Transition," *AIAA Journal*, Vol. 44, No. 5, May 2006, pp. 1009–1024. doi:10.2514/1.12431
[51] Tysell, L. G., "Adaptive Grid Generation for 3D Unstructured Grids," *Proceedings to Numerical Grid Generation in Computational Field Simulations. International Society of Grid Generation (ISGG)*, Greenwich, England, U.K., 1998, pp. 391–400.
[52] Eliasson, P., "Edge, a Navier–Stokes Solver for Unstructured Grids," *Proceedings of Finite Volumes for Complex Applications 3*, 2002, pp. 527–534.
[53] Thomas, P. D., and Lombard, C. K., "Geometric Conservation Law and its Application to Flow Computations on Moving Grids," *AIAA Journal*, Vol. 17, No. 10, 1979, pp. 1030–1037. doi:10.2514/3.61273
[54] Bartels, R. E., "Finite Macro-Element Mesh Deformation in a Structured Multi-Block Navier–Stokes Code," NASA TM 213789, 2005.
[55] de Boer, A., van der Schoot, M., and Bijl, H., "Mesh Deformation Based on Radial Basis Function Interpolation," *Computers and Structures*, Vol. 85, Nos. 11–14, 2007, pp. 784–795. doi:10.1016/j.compstruc.2007.01.013
[56] Zeng, D., and Ethier, C. R., "A Semi-Torsional Analogy Model for Updating Unstructured Meshes in 3D Moving Domains," *Finite Element in Analysis and Design*, Vol. 41, Nos. 11–12, 2005, pp. 1118–1139. doi:10.1016/j.finel.2005.01.003
[57] Stephens, C. H., Arena, A. S., and Gupta, K. K., "Application of the Transpiration Method for Aeroservoelastic Prediction Using CFD," AIAA TR 98-2071, 1998.
[58] Stephens, C. H., Arena, A. S., and Gupta, K. K., "CFD-Based Aeroservoelastic Predictions with Comparison to Benchmark Experimental Data," AIAA TR 99-0766, 1999.
[59] Gao, C., Luo, S., and Schuster, D., "Calculation of Unsteady Transonic Flow by an Euler Method with Small Perturbation Boundary Condition," AIAA Paper 03-1267, 2003.
[60] Maman, N., and Farhat, C., "Matching Fluid and Structure Meshes for Aeroelastic Computations: A Parallel Approach," *Computers and Structures*, Vol. 54, No. 4, 1995, pp. 779–785. doi:10.1016/0045-7949(94)00359-B
[61] Lancaster, P., and Salkauskas, K., "Surfaces Generated by Moving Least Squares Methods," *Mathematics of Computation*, Vol. 37,

No. 155, 1981, pp. 141–158.
doi:10.1090/S0025-5718-1981-0616367-1

[62] Schaback, R., "Remarks on Meshless Local Construction of Surfaces," *Proceedings of IMA Mathematics of Surfaces IX Conference*, Cambridge, England, U.K., 2000, pp. 34–58.

[63] Wendland, H., "Piecewise Polynomial, Positive Definite and Compactly Supported Radial Functions of Minimal Degree," *Advances in Computational Mathematics*, Vol. 4, No. 1, 1995, pp. 389–396.
doi:10.1007/BF02123482

[64] Yates, E. C., "AGARD Standard Aeroelastic Configurations for Dynamic Response. I Wing 445.6," AGARD, R 765, 1985.

[65] Ewins, D. J., *Modal Testing: Theory, Practice and Application (Mechanical Engineering Research Studies Engineering Design Series)*, Taylor and Francis, Philadelphia, PA, Feb. 2003.

[66] Raveh, D. E., Karpel, M., and Yaniv, S., "Nonlinear Design Loads for Maneuvering Elastic Aircraft," *Journal of Aircraft*, Vol. 37, No. 2, March–April 2000, pp. 313–318.
doi:10.2514/2.2595